

DIRECT NUMERICAL SIMULATION OF DILUTE SUSPENSION PARTICLE-LADEN GRAVITY CURRENTS

Luis F. R. Espath

Faculdade de Engenharia
Pontifícia Universidade Católica do Rio Grande do Sul
Av. Ipiranga 6681, 90619-900 Porto Alegre - RS, Brasil
espath@gmail.com

Leandro C. Pinto

Faculdade de Engenharia
Pontifícia Universidade Católica do Rio Grande do Sul
Av. Ipiranga 6681, 90619-900 Porto Alegre - RS, Brasil
leandroconp@gmail.com

Sylvain Laizet

Turbulence, Mixing and Flow Control Group, Department of Aeronautics
Imperial College London, London, SW7 2BY, United Kingdom
sylvain.laizet@gmail.com

Jorge H. Silvestrini

Faculdade de Engenharia
Pontifícia Universidade Católica do Rio Grande do Sul
Av. Ipiranga 6681, 90619-900 Porto Alegre - RS, Brasil
jorgehs@pucri.br

ABSTRACT

For this numerical work, we are interested in the prediction of a mono-disperse dilute suspension particle-laden flow in the typical lock-exchange configuration. The main objective is to investigate the influence of the Reynolds number in such flows. 2D and 3D Direct Numerical Simulations (DNS) with three different Reynolds numbers are presented with comparisons with previous experimental and numerical works.

INTRODUCTION

Gravity currents are very common in nature, either in atmosphere due to sea-breeze fronts, in mountain avalanches of airborne snow or debris flow, or in the ocean due to turbidity currents or river plumes (Simpson, 1982). In this numerical study, we focus on particle-laden hyperpycnal flows, with negative-buoyancy, where dynamics play a central role in the formation of hydrocarbon reservoirs (Meiburg and Kneller, 2009). Moreover, these particle-driven gravity currents are often extremely dangerous for the stability of submarine structures placed at the sea-floor like pipelines or submarines cables. It is clear that the understanding of the physical mechanism associated with these currents as well as the correct prediction of their main features are of great importance for practical and theoretical purposes. For this work, we

are interested in the prediction of a mono-disperse dilute suspension particle-laden flow in the typical lock-exchange configuration. We consider only flat surfaces using DNS (Direct Numerical Simulation). Our approach takes into account the possibility of particles deposition but ignores erosion and/or re-suspension. Note that in dilute suspensions, the particle volume fraction is considered relatively small, typically well below 1%.

Previous results for this kind of flows were obtained in laboratory experiments (de Rooij and Dalziel, 2001; Gladstone *et al.*, 1998), using simplified theoretical models (Rottman and Simpson, 1993; Bonnezaze *et al.*, 1993), or by numerical simulations (Necker *et al.*, 2002; Necker *et al.*, 2005; Nasr-Azadani *et al.*, 2011). It was shown that boundary conditions, initial conditions associated with the lock configuration, and particle sizes can have a strong influence on the main characteristics of this kind of flows.

The principal objective of this numerical study is to investigate the turbulence structures in such flows for various Reynolds numbers for bi- and three-dimensional configurations. Particularly, we will focus on changes occurring in the current front. The main features of the flow are related with the temporal evolution of the front location as well as the suspended sediment mass, sedimentation rate, and the resulting streamwise deposit profiles.

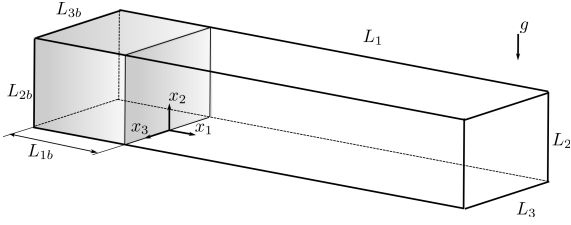


Figure 1: Schematic view of the initial configuration of the lock-exchange flow problem.

FLOW CONFIGURATION AND EQUATIONS

The lock-exchange flow configuration is used (Figure 1) where uniformly suspended particle sediments are enclosed in a small portion of the dimension domain $L_{1b} \times L_{2b} \times L_{3b}$ separated by a gate with clear fluid. When the gate is removed the particle-fluid mixture flows due to gravity and it undergoes a mutual inverse interaction between the "heavy" particle-mixture flow and the "light" clear fluid. We assume a dilute suspension of single diameter particles and we do not take into account the influence of particle inertia and/or particle-particle interaction.

With the restriction imposed by the dilute suspension approach, this flow can be evaluated numerically by solving the Navier-Stokes and scalar transport equations under the Boussinesq approximation. To make these equations dimensionless, half of the box height is chosen (Figure 1) as the characteristic length scale h and the buoyancy velocity u_b is chosen as the velocity scale. The buoyancy velocity is related to the reduced gravitational acceleration $u_b = \sqrt{g'h}$ where $g' = g(\rho_p - \rho_0)c_i/\rho_0$. The particle and clear fluid densities are ρ_p, ρ_0 respectively, with g being the gravitational acceleration and c_i the initial volume fraction of the particles in the lock. When introducing the velocity and length scales two dimensionless numbers appear in the equations: the Reynolds number defined as $Re = u_b h/\nu$ where ν is the kinematic viscosity of the fluid, and the Schmidt number $Sc = \nu/k$, where k is the mass diffusivity of the particle-fluid mixture. All other parameters and variables are made dimensionless using c_i, h or/and u_b . Thus, the dimensionless form for the governing equations are

$$\frac{\partial u_l}{\partial x_l} = 0, \quad (1a)$$

$$\frac{\partial u_i}{\partial t} + u_l \frac{\partial u_i}{\partial x_l} = -\frac{\partial p}{\partial x_l} + \frac{2}{Re} \frac{\partial s_{il}}{\partial x_l} + c e_i^g, \quad (1b)$$

$$\frac{\partial c}{\partial t} + (u_l + u_s e_l^g) \frac{\partial c}{\partial x_l} = \frac{1}{Sc Re} \frac{\partial^2 c}{\partial x_l^2}, \quad (1c)$$

where $e_l^g = (0, -1, 0)$ is the unit vector in gravity direction and the nondimensional quantities u_i, p, c, s_{il} represent the fluid velocity, pressure, particle concentration and strain rate tensor, respectively. The particle settling velocity u_s is related to the particle diameter by the Stokes settling velocity law.

Table 1: Summary of numerical parameters.

Re	L_1, L_2, L_3	n_1, n_2, n_3	Δt
2236	2D	18, 2	1×10^{-3}
	3D	18, 2, 2	6.024×10^{-4}
5000	2D	18, 2	5×10^{-4}
	3D	18, 2, 2	5×10^{-4}
10000	2D	18, 2	3×10^{-4}
	3D	18, 2, 2	3×10^{-4}

Initial conditions are defined introducing a weak perturbation on the velocity field in the neighbourhood of the interface in order to mimic the disturbances introduced in the flow when the mixture is released. Free-slip boundary conditions are imposed for the velocity field in the streamwise and spanwise directions. No-slip boundary conditions are used in the vertical direction. For the scalar, no-flux conditions are used in the streamwise and spanwise directions and in the vertical direction at the top of the domain. In order to take into account the particles deposit in the vertical direction at the bottom of the domain, an outflow boundary condition is used, $\frac{\partial c}{\partial t} + u_s e_2^g \frac{\partial c}{\partial x_2} = 0$, which allows particles to leave the computational domain mimicking a deposition process. It should be noticed that no re-suspension is allowed.

NUMERICAL METHOD AND PARAMETERS

In order to solve numerically the governing equations (1a,1b,1c) the in-house code `Incompact3d` developed by Laizet and Lamballais (2009) is used. It is based on compact sixth-order finite difference schemes for spatial differentiation and a third-order Adams-Bashforth scheme for time integration. To treat the incompressibility condition, a fractional step method requires to solve a Poisson equation. This equation is fully solved in spectral space via the use of relevant 3D Fast Fourier Transforms. More information about the code can be found in Laizet and Lamballais (2009). For the three-dimensional simulations presented here, the parallel version of `Incompact3d`, based on a powerful 2D domain decomposition is used. More details about this domain decomposition can be found in Laizet and Li (2011). The two-dimensional simulations are performed with the vector version of the code.

The numbers of mesh nodes and the size of the simulations are presented in Table 1. We consider $(L_{1b}, L_{2b}, L_{3b}) = (1, 2, 2)$ to define the box containing the particle-fluid mixture. The settling velocity is set to $u_s = 0.02$ in order to correspond with a middle silt while the Schmidt number is fixed in $Sc = 1$. All the simulations were run for $t = 60$ except the $Re = 10000$ which was stopped at $t = 32$ in order to limit the computational effort. The perturbation added to the initial velocity field is adjusted to yield an initial kinetic energy 1% of the initial potential energy.

It should be noted that the $Re = 2236$ case is sim-

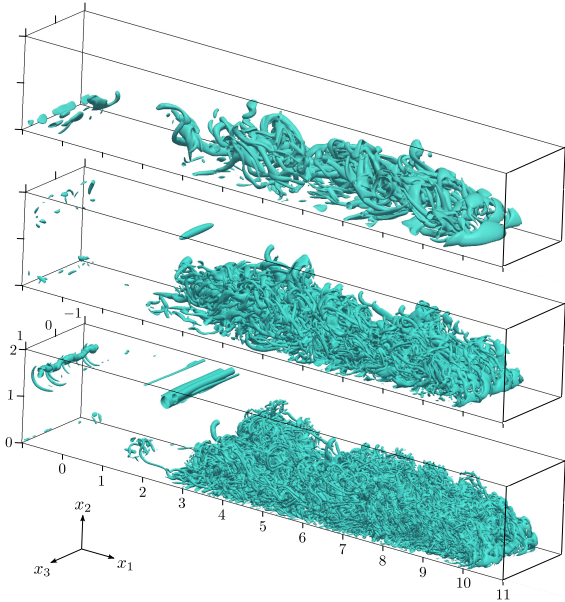


Figure 2: Turbulent structure of the gravity currents by isosurfaces of Q -criterion (for the isovalue $Q = 1$) for $Re = 2236, 5000, 10000$ (from top to bottom) at $t = 20$.

ilar to the numerical work of Necker *et al.* (2002). The only difference lies in the way the weak perturbation is added as initial condition to the velocity field. The $Re = 10000$ case is very close to the experimental configuration of de Rooij and Dalziel (2001).

RESULTS

In this section, a selection of results concerning analysis of instantaneous visualizations of the flow, global quantities associated with front location and runout length, suspended material, and streamwise particle deposits is presented. The focus is on the description of the main features of the gravity current front characterized by the so-called lobe-and-cleft instability (Härtel *et al.*, 2000b) and on the spatial distribution of the shear stress over the channel bottom.

Instantaneous visualization

The sudden release of the particle-fluid mixture along the left wall (figure 1) leads to the streamwise evolution of the gravity current into the clear fluid. Due to the small amount of kinetic energy at $t = 0$, this motion is initially two-dimensional (not shown here) then further downstream three-dimensional structures can be observed at the head and at the tail of the current. At $t = 20$ the gravity current develops a highly 3D turbulence with intense streamwise vortices as shown with the Q -criterion from Figure 2. The pictures are taken with the same isovalue ($Q = 1$). Therefore, it can be seen a higher level of turbulence with smaller and very intense structures for the $Re = 10000$ simulation by comparison with the lower Re simulations.

In Figure 3 snapshots of the concentration field

are shown at $t = 20$ for the two-dimensional (left) and the $x_3 = 0$ middle-plane for the three-dimensional (right) simulations for the three Re numbers considered. The picture shows important differences between the 2D and 3D simulations concerning mainly the front location, the development of Kelvin-Helmholtz instability and the resulting vorticity structures. Furthermore, due to particle settling, high levels of particle concentration are located near the wall. However, in the 2D results it can be seen that high levels of concentration are trapped by the vorticity located at the tail of the current. This result denotes that the particle mass should remain suspended for longer time for the 2D case. The particle concentration fields for the 3D simulations also show that when the Reynolds number is increased, the suspended mass is decreased. This point will be addressed in the following.

Global results

The temporal evolution for the front location, suspended particles mass, sedimentation rate and deposit profiles at the bottom of the box are compared with the numerical predictions obtained by Necker *et al.* (2002) and with the experimental data of de Rooij and Dalziel (2001). Figure 4 shows the time evolution of the front location, x_f , and of the suspended mass normalized by the initial suspended mass, m_p/m_{p0} , for all the simulations. From figure 4 it can be observed that the particle-driven current has a constant front velocity until time $t \approx 10$, similar to density-driven current without particles as shown in Härtel *et al.* (2000a). After $t \approx 10$ the front velocity deviates from the straight line due to particles settling. The overall agreement for both, front location and suspended mass, is reasonably good with the data of Necker *et al.* (2002). The small differences can be related to the perturbations added as initial conditions on the velocity field. Given that gravity currents in lock-exchange configurations are mostly transient flows, it can be expected that the front location results are more influenced by the initial conditions than by the Re number. Nevertheless, there is a clear tendency for an increasing front velocity for increasing Reynolds numbers. The suspended mass for the 3D simulations follows what was observed in the particle concentration pictures (figure 3), with less suspended sediments computed for the highest Re simulation and for 2D cases as well. These results can also be checked by computing the time evolution of sedimentation rate

$$\dot{m}_s = \frac{1}{L_1 L_3} \int_0^{L_1} \int_0^{L_3} c_w(x_1, x_3, t) u_s dx_3 dx_1, \quad (2)$$

as it is shown in figure 5 for the 2D (top) and the 3D (bottom) simulations. In Equation (2), c_w accounts for the sediment concentration at the bottom channel. Although the sedimentation rate is strongly affected by the initial condition, good agreement is also

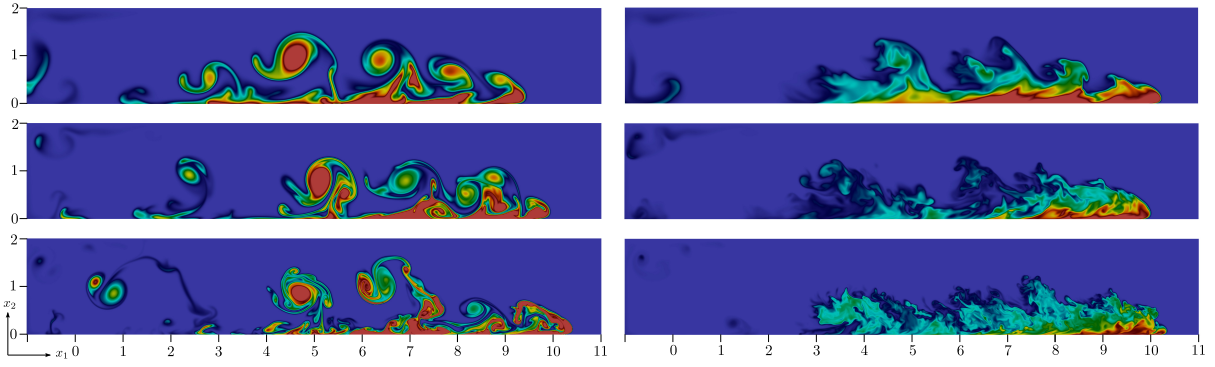


Figure 3: Particle concentration fields at $t = 20$ for $Re = 2236, 5000, 10000$ (from top to bottom) for the 2D (left) and the $x_3 = 0$ middle plane for the 3D (right) configurations. Snapshots taken for $0 < c < 0.3$.

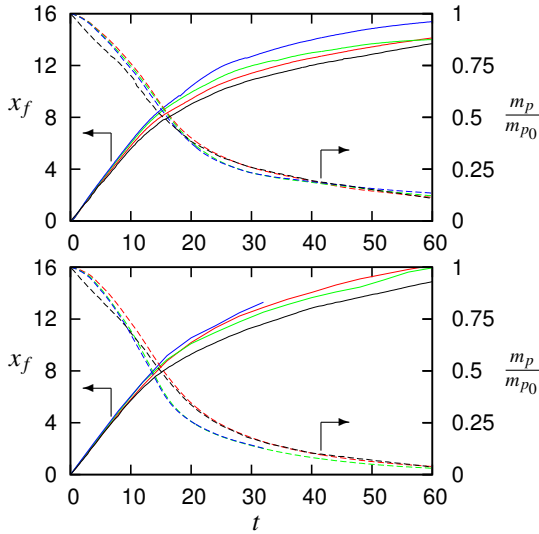


Figure 4: Front location x_f and suspended particles m_p/m_{p0} as a function of time for the 2D (top) and the 3D (bottom) configurations: red, green and blue lines are referred, respectively, to $Re = 2236, 5000, 10000$ and black lines to the numerical data of Necker *et al.* (2002).

observed with the 2D and the 3D numerical predictions of Necker *et al.* (2002) for $Re = 2236$. For the 2D configuration, the curve shows a peak value around $t \approx 15$, independent of Re . When this happens $\approx 50\%$ of the suspended particles are already settled (figure 4). For the 3D case the sedimentation rate curve experiments a time shift accelerating the deposition when the Re number is increased. In all cases the time evolution of the sedimentation rate follows a power law with positive and negative exponent before and after the peak value with similar trend as the numerical data. Finally, it should be noticed that for the sedimentation rate the difference between $Re = 5000$ and $Re = 10000$ is very small.

Another global quantity of extremely importance for practical implications is the streamwise deposit of sediment particles computed as

$$D_t(x_1, t) = \int_0^t \langle c_w(x_1, \tau) \rangle_{x_3} u_s d\tau, \quad (3)$$

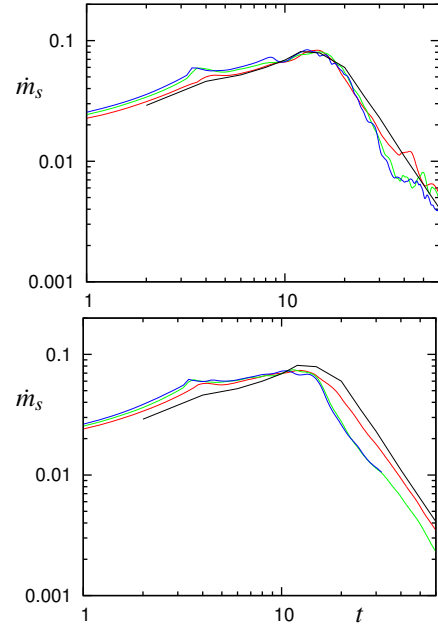


Figure 5: Sedimentation rate $\dot{m}_s(t)$ as function of time for 2D (top) and 3D (bottom) configurations: red, green and blue lines are referred, respectively, to $Re = 2236, 5000, 10000$ and black lines to the numerical data of Necker *et al.* (2002).

where $\langle \cdot \rangle_{x_3}$ indicated a mean value in the x_3 direction. Figure 6 shows this quantity in function of the streamwise coordinate x_1 . The deposit is normalized with the deposit for the final time $t = 60$. For the 2D (top of figure 6) and the 3D cases (bottom of figure 6) the selected times are $t = 7.3, 10.95, 60$. Note that the 3D DNS for $Re = 10000$ was stopped at $t = 32$ to limit the computational effort. With this choice, the present results may be compared both with the numerical data of Necker *et al.* (2002) and the experimental data of de Rooij and Dalziel (2001). A global agreement between experimental data and numerical results can be seen in this figure. Our 2D simulations seem to overestimate the deposit at the end of the simulation. The top picture of figure 6 shows that 2D simulations are giving incorrect prediction for high values of the deposit. On the other hand, the 3D results for $Re = 5000$ (green one) are very close to the experimental data

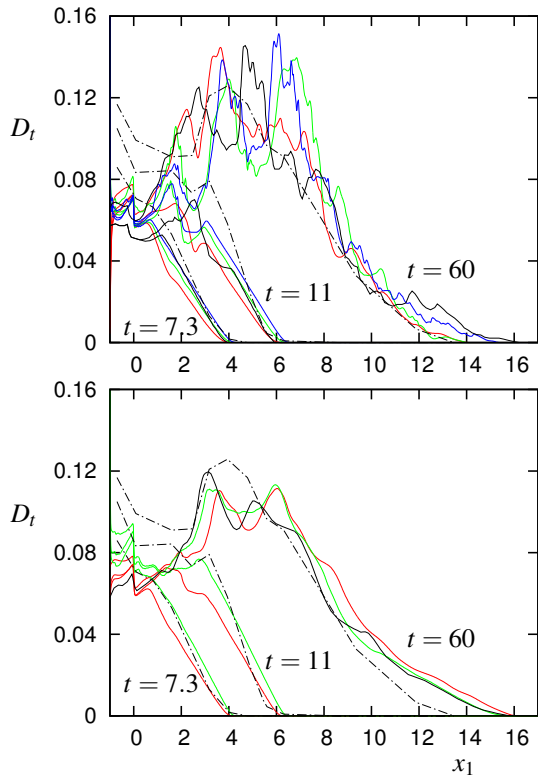


Figure 6: Deposit profiles for $t = 7.3, 11, 60$ for the 2D (top) and the 3D (bottom) simulations: red, green and blue lines correspond to, respectively $Re = 2236, 5000, 10000$, black solid lines to the numerical data of Necker *et al.* (2002) and black dashed line to the experimental data of de Rooij and Dalziel (2001).

both at initial and final times of the simulation. The differences at the left channel side can be attributed to different initial conditions between laboratory experiments and numerical simulations.

Wall turbulence characteristics

At the bottom wall of the channel, increasing spanwise motions cause lobe-and-cleft structures at the current front location. This complex structure was observed in many experiments (Simpson, 1972) and more recently in the DNS of density-driven current (without suspended particles) of Härtel *et al.* (2000b) and the particle-driven simulations of Necker *et al.* (2002). In Figure 7, the wall shear velocity field at the wall is shown for $t = 8$, computed as $|s|_w = \sqrt{(\partial u_1 / \partial x_2)^2 + (\partial u_3 / \partial x_2)^2}|_{x_2=0}$, for the three Re considered in this numerical work. The same color distribution was used for the three pictures. The front structure (which seems a *dental radiography*) is readily seen. It is formed by zones of high shear velocity, the lobe region, alternating with regions of low values, the cleft region. This spatial organization of the wall shear velocity can be correlated with other physical phenomena, not considered in the present simulations. Regions of intense vertical gradient are good candidates to undergo local erosion processes. More intense activity at the front but also

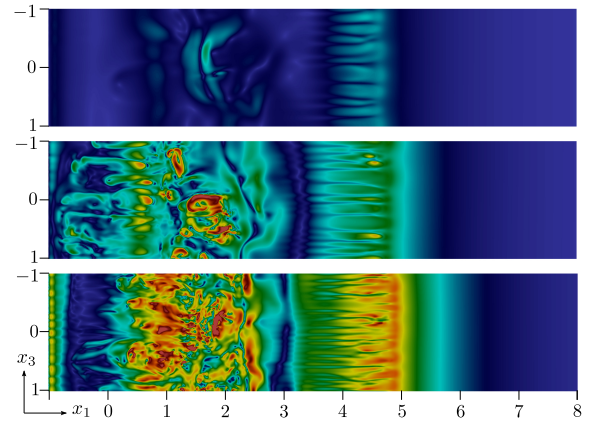


Figure 7: Wall shear velocity at $t = 8$ for $Re = 2236, 5000, 10000$ (from top to bottom). Same color distribution for all pictures with $0 < |s|_w < 1000$.

for $0.5 < x_1 < 2.5$ can be observed when the Re number is increased.

Härtel *et al.* (2000) showed that the initial 2D base flow, without suspended particles, is linearly unstable to small 3D perturbations. These perturbations are the seed of the lobe-and-cleft instability that characterizes the 3D behaviour of the current front. The linear stability analysis, developed by the authors, shows that the spanwise wavenumber $\beta = 2\pi/l_\beta$ and the amplification rate of most unstable mode are function of the Grashof number ($Gr = Re^2$). Here l_β is the characteristic spanwise wavelength of the lobe-and-cleft instability. Considering our three simulations, the following theoretical results are obtained: $l_\beta = 0.196, 0.125, 0.084$ for $Re = 2236, 5000, 10000$ respectively. For comparison purposes, in present simulations a x_1 location plane was selected just behind the front at the early stage of the gravity current ($t = 4$ for $Re = 2236$ and $t = 2.6$ for $Re = 5000, 10000$). In these planes, Fast Fourier Transforms analysis of vertical velocity in x_3 gives $l_\beta = 0.2, 0.111, 0.083$ respectively, with values very close to the theoretical ones.

At $t = 8$ the structure of the particle-laden gravity current front can be analysed through the visualization of the concentration field as it is shown on the left side picture of Figure 8. The isovalue chosen is $c = 0.25$. At the right side of the same picture, a cross section of Q -criterion for the selected vertical planes just behind the current front is shown (figure 8). From this figure, the lobe-and-cleft instability can be already identified in the region limited by pairs of streamwise vortices associated with positive values of Q -criterion (indicated in red). The picture also shows how these streamwise vortices become thinner and more intense when the Re number is increased. Also in the picture, the blue zone, where $Q < 0$, denotes a region where the strain rate overcomes the rotation rate. Figures 7 and 8 suggest that clefts are related to high strain rate region whereas lobes are limited by zones of intense streamwise vorticity.

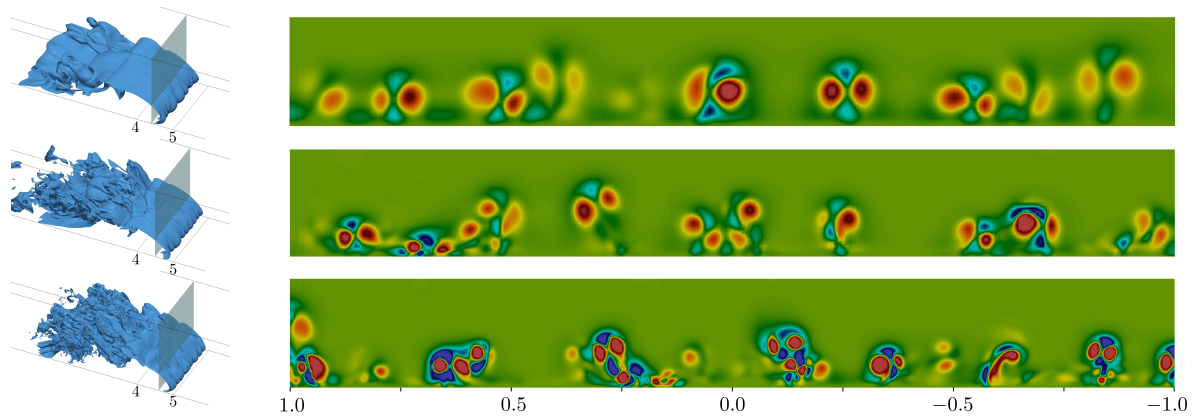


Figure 8: Structure of the front by isosurface for $c = 0.25$ (left) and Q -criterion with an isovalue ranging from $-25 < Q < 25$ (right) for $Re = 2236, 5000, 10000$ (from top to bottom) at $t = 8$.

CONCLUSION

The main features of a particle-driven gravity current for a dilute suspension in a lock-exchange configuration were examined using 2D and 3D DNS. Three Re numbers were considered allowing direct comparisons with published experimental and numerical data. The main results are related with the streamwise length and suspended sediment mass of the current front, the time evolution of sedimentation rate and the resulting particle deposit at the channel wall. Good global agreements were found with published results. In present simulations, no erosion and/or re-suspension processes were considered. Nevertheless, the prediction of the spatial and temporal flow structure at the wall may be related to local erosion processes through the identification of region of high shear velocity or streamwise vorticity (the lobe zone). On the other hand, high strain rate are located at the cleft region.

ACKNOWLEDGEMENTS

Present simulations have been carried out at the LAD/PUCRS in Porto Alegre. The authors are grateful to Petrobras for supporting this research. JS acknowledges financial assistance of CNPq.

REFERENCES

- BONNECAZE, R., HUPPERT, H. & LISTER, J. 1993 Particle-driven gravity currents. *J. Fluid Mech.* **250**, 339–369.
- DE ROOIJ, F. & DALZIEL, S. 2001 Time- and space-resolved measurements of deposition under turbidity currents. *Spec. Publ. Int. Ass. Sediment.* **31**, 207–215.
- GLADSTONE, C., PHILLIPS, J. & SPARKS, R. 1998 Experiments on bidisperse, constant-volume gravity currents: propagation and sediment deposition. *Sedimentology* **45**, 833–843.
- HÄRTEL, C., CARLSSON, F. & THUNBLUM, M. 2000a Analysis and direct numerical simulation of

- the flow at a gravity-current head. Part 2. The lobe-and-cleft instability. *J. Fluid Mech.* **418**, 213–229.
- HÄRTEL, C., MEIBURG, E. & NECKER, F. 2000b Analysis and direct numerical simulation of the flow at a gravity-current head. Part 1. Flow topology and front speed for slip and no-slip boundaries. *J. Fluid Mech.* **418**, 189–212.
- LAIZET, S. & LAMBALLAIS, E. 2009 High-order compact schemes for incompressible flows: A simple and efficient method with the quasi-spectral accuracy. *J. Comp. Phys.* **228**, 5989–6015.
- LAIZET, S. & LI, N. 2011 Incompact3d: A powerful tool to tackle turbulence problems with up to $O(10^5)$ computational cores. *Int. J. Heat and Fluid Flow* **67**, 1735–1757.
- MEIBURG, E. & KNELLER, B. 2009 Turbidity currents and their deposits. *Annu. Rev. Fluid Mech.* **42**, 135–156.
- NASH-AZADANI, M., HALL, B. & MEIBURG, E. 2011 Polydisperse turbidity currents propagating over complex topography: Comparison of experimental and depth-resolved simulation results. *Computers and Geosciences*, doi:10.1016/j.cageo.2011.08.030.
- NECKER, F., HÄRTEL, C., KLEISER, L. & MEIBURG, E. 2002 High-resolution simulations of particle-driven gravity currents. *Int. J. Multiphase Flow* **28**, 279–300.
- NECKER, F., HÄRTEL, C., KLEISER, L. & MEIBURG, E. 2005 Mixing and dissipation in particle-driven gravity currents. *J. Fluid Mech.* **545**, 339–372.
- ROTTMAN, J. & SIMPSON, J. 1983 Gravity currents produced by instantaneous releases of a heavy fluid in a rectangular channel. *J. Fluid Mech.* **135**, 95–110.
- SIMPSON, J. E. 1982 Gravity currents in the laboratory, atmosphere and ocean. *Annu. Rev. Fluid Mech.* **14**, 213–234.
- SIMPSON, J. E. 1972 Effects of the lower boundary on the head of a gravity current. *J. Fluid Mech.* **53**, 759–768.